RESEARCH ARTICLE

High-Precision External Parameter Calibration Method for Camera and Lidar Based on a Calibration Device

SONG FAN[1,2]**, YING YU**[1]**, MAOLIN XU**[2]**, AND LONGHAI ZHAO**[3]

[1]School of Geospatial Information, PLA Information Engineering University, Zhengzhou 450001, China
[2]School of Civil Engineering, University of Science and Technology Liaoning, Anshan 114000, China
[3]32016 Troops, Lanzhou 730000, China

Corresponding author: Ying Yu (yuying5559104@163.com)

ABSTRACT The fusion of camera and lidar plays an important role in the field of robotic perception. The accurate external parameter calibration is a necessary prerequisite for sensor fusion. Herein, an auxiliary calibration device with distinctive geometric features was designed to address the problems of low accuracy and poor robustness associated with external parameter calibrations of camera and lidar. Moreover, a coarse-to-fine two-stage calibration method was proposed for the external parameters of the camera and lidar. The first stage of the method is the extraction of multiple groups of two-dimensional (2D) and three-dimensional (3D) lines corresponding to the edge of the calibration device from the image and lidar point cloud that yields a unique initial estimation of the external parameters. In the second stage, the 2D–3D center point of the sphere of the calibration device was detected, and the initial external parameters were further optimized using a nonlinear optimization method. The proposed method provides two different features that add stability against noise to the calibration system. Both simulated and actual experiments show that the method can yield high-precision external parameters without an initial value. Compared to state-of-the-art methods, our method has advantages in terms of accuracy. the calibration system has a certain degree of noise resistance and stability under different laser noise and vertical resolution.

INDEX TERMS Calibration device, camera and lidar fusion, external parameter calibration, nonlinear optimization.

I. INTRODUCTION

Concomitant with the rapid development of robotics and sensor technology, more stringent performance criteria are being assigned to robotic perception. Based on their roles as the "eyes" of robots, vision and Light Detection and Ranging (lidar) sensors assume the function of environmental perception. In a complex environment, it is difficult for a single sensor to meet the perception requirements demanded by certain scenarios. Sensor fusion technology has become a reliable solution for achieving a richer perception spectrum. A camera can provide pixel information with a rich texture but

The associate editor coordinating the review of this manuscript and approving it for publication was Mauro Gaggero .

lacks actual three-dimensional (3D) information. Conversely, although lidar can obtain accurate 3D information, its spatial resolution is low. The fusion of the information acquired from a camera and lidar mitigates the limitations inherent in the respective sensors, combines their respective advantages, and improves the overall perception of the environment. The calibration of external spatial parameters constitutes an important step in the fusion of a camera and lidar, and aims at obtaining a rigid-body transformation relation between the respective sensors' coordinate systems. This study explored the external parameter calibration of a camera and lidar using a specific calibration device.

The specific aims of this study were to establish the corresponding relations between common features of the

field-of-view ("view features"), consisting of points, lines, surfaces, and vectors. However, it is difficult to extract common view features from point clouds. First, the point clouds collected by lidar are sparse, and it is difficult to detect corresponding features; second, the existence of point-cloud noise affects the accuracy of feature fitting. Therefore, special calibrators are typically used to assist in feature extraction. External parameter calibration methods using a calibration object are generally called target-based methods. The most representative target-based method is the chessboard pattern calibration method, which provides a variety of common view features, such as the correspondence of plane-normal vectors [1], the 2D–3D correspondence of the chessboard corners [2], and the 2D–3D correspondence of plane masks [3]. In addition to the chessboard calibration method, other calibration objects, such as trihedrons [4], ArUco calibration boards [5], and spheres [6], also assist in extracting the corresponding common view features. Target-based methods are suitable for indoor or static scenes, and often obtain satisfactory calibration results.

In contrast to target-based methods, targetless methods don't need the aid of calibration objects. These methods typically extract features directly from the environment for external parameter calibration. Examples of targetless methods include motion-based [7], mutual information- methods [8], feature-based [9], and deep-learning-based methods [10]. Targetless methods avoid the constraints imposed by a particular calibration object, decrease the cost of the calibration and render the calibration process more convenient. However, stricter requirements adhere to the calibration scene, and the initial values of the external parameters have a substantial effect on the calibration results. Therefore, the stability and accuracy of targetless methods often inferior to those of target-based methods [3].

To sum up, targetless methods pay more attention to flexible calibration test, while target-based methods reflect the stability and accuracy of calibration. However, in the research of target detection and SLAM, the accuracy of calibration is obviously more important.
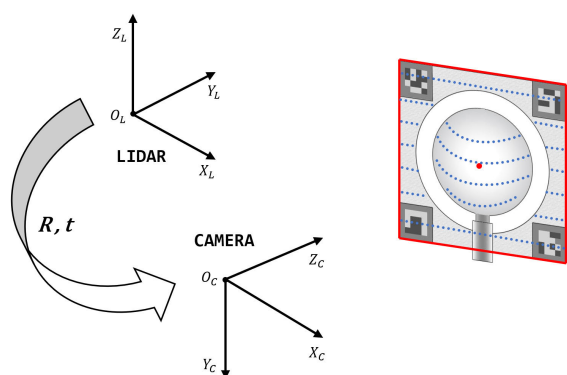
FIGURE 1. Rigid-body transformation relation between the camera and lidar coordinate systems.

In this work, we propose a high-precision external parameter calibration method for camera and lidar based on specific calibration equipment, which combines the advantages of calibration based on sphere and calibration plate. Note that this is different from the method proposed in [5] and [6]. These methods use a single common view feature as the input, and when there is interference in the observation, the calibration may fall into the local optimum and affect the final result. Therefore, we extract two different features for two-stage optimization, avoiding the optimization falling into local optimum, so as to ensure the stability and accuracy of the required calibration. The calibration process and the external parameters to be calibrated are shown in Figure 1. First, a new calibration device is designed. Its main body is composed of a sphere and a hollowed calibration plate. Second, the common viewpoint and line features in the image and point cloud are automatically extracted. Finally, considering the correspondence of 2D–3D lines and points, a two-stage calibration framework ranging from coarse to fine is proposed to estimate accurately the external parameters from the lidar to the camera coordinate system without using an initial value a priori. Parameters R and t represent the rotation and translation matrices, respectively.

II. RELATED WORK

As explained in the previous section, camera-and-lidar external parameter calibration methods can be divided into targetless and target-based methods. Targetless methods do not depend on specific calibration objects. They predominantly extract features from the environment itself and use these features to calculate the relation between the spatial positions of the camera and lidar. Ishikawa et al. [11] used a sensor fusion odometer to apply the hand–eye calibration framework to 2D–3D calibration to the process of motion, but the scale uncertainty of the visual odometer affected the calibration accuracy in that study. Kang et al. [12] proposed a cost function that minimized the alignment of observation edges to estimate external parameters; however, that method required more accurate initial values of the external parameters and an adaptive environment to avoid the optimization from falling into localized optimization minima. Pandey et al. [13] used the relation between the reflectivity of the lidar point cloud and the grayscale of the image to optimize the external parameters by maximizing the mutual statistical information. However, that method was significantly affected by light and burdened by strict environmental requirements. External parameter calibration of cameras and lidars has also been studied in the field of deep learning [10], [14]. Automatic calibration of external parameters can be achieved using training networks; however, this method lacks universality for different scenes. Although the targetless method has the advantage of a high degree of automation, it is constrained by particular limitations that affect calibration accuracy.

In contrast to the targetless methods reviewed in the preceding paragraph, target-based calibration methods usually employ a calibration device to calibrate the external parameters by extracting the geometric features of the calibration device. The calibration results obtained for different
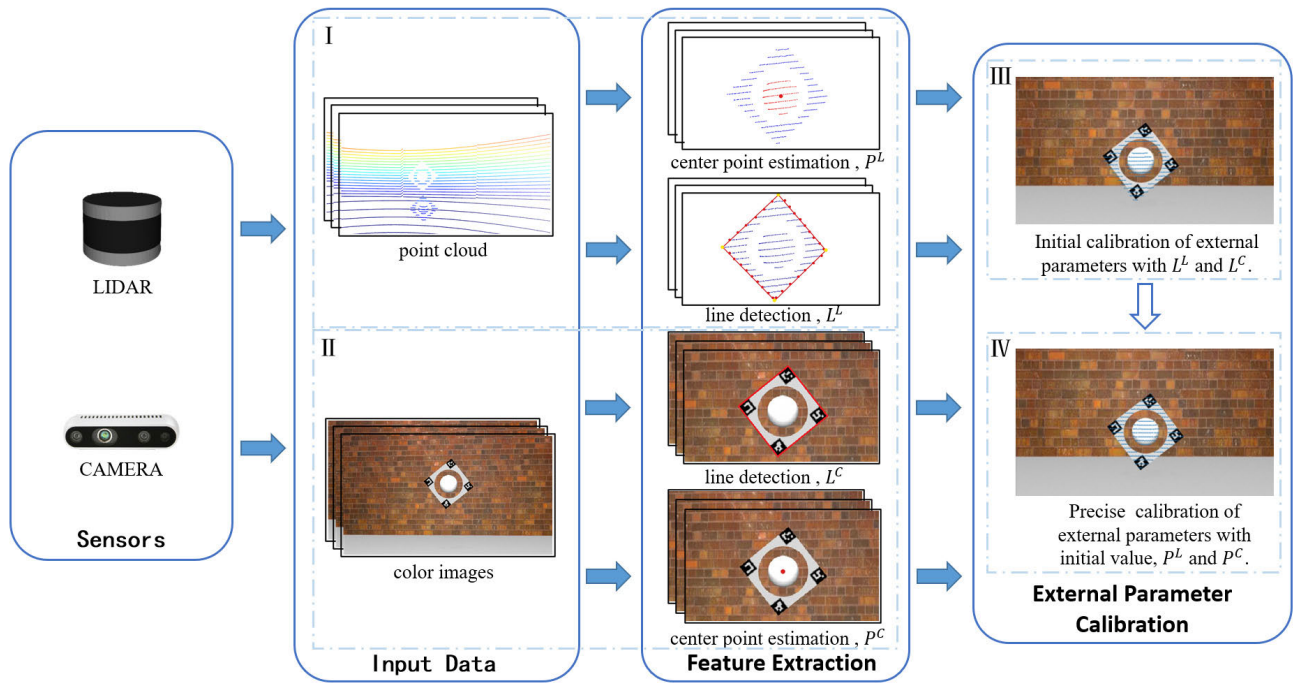
FIGURE 2. Rigid-body transformation relation between the camera and lidar coordinate systems.

calibration targets are often slightly different. Among these, the chessboard, which is conducive to visual extraction, is the most extensively used. Its core aim is to extract 3D–3D or 2D–3D corresponding features and estimate the external parameters. Wang et al. [15] calibrated the spatial relationship between lidar and panoramic cameras using the correlation of the reflection intensity of the lidar point cloud with the color of the chessboard pattern. Tsai et al. [16] proposed a variable quality index to score each group of calibration samples using a chessboard. This scoring mechanism optimally adapted the calibration parameters to the entire scenario. Additional research has been conducted on calibration objects. Gong et al. [4] used an arbitrary trihedron, Park et al. [17] used multiple groups of polygonal calibration plates, Pusztai and Hajder [18] used cardboard boxes, and Beltrán et al. [19] used a hollow circular design. These methods yielded satisfactory calibration results. Spheres have also been applied in previous studies [6], [20]. Spheres allow the extraction of correspondence relationships of the spherical centers in images and point clouds and are not affected by the observation angle. Based on the aforementioned methods, the main purpose of different forms of processing of the calibration object is to obtain accurate corresponding features. Because the accuracy of feature extraction often determines the final calibration accuracy, the factors that affect the accuracy of feature extraction include the sparsity of point clouds, point-cloud noise, and the manufacturing accuracy of the calibration device. Therefore, a good calibration scheme must consider both a precise calibration object design and control of the effect of the calibration algorithm on noise and other influencing factors. In this study, we investigated

a camera-and-lidar calibration method, based on a novel calibration device that is robust to the sparsity and noise of point clouds.

III. OVERVIEW AND METHODOLOGY

A flowchart of our method is illustrated in Figure 2. The entire calibration process is divided into four parts. The first part constitutes the lidar point-cloud feature extraction with the PCL library. First, we set the spatial range of the calibration field and used a statistical filtering algorithm to remove obvious outlier point clouds. Second, we performed reflection-intensity filtering and RANSAC plane extraction on the remaining point clouds to obtain point-cloud clusters on the sphere and the plane. Finally, we fitted the point cloud on the sphere to obtain the sphere's center coordinates, wherein the α-shape algorithm extracted the plane-edge point cloud and then fitted the straight-line features of the four sides of the calibration plate. The second part of our method applied image feature extraction using the ArUco module of OpenCV to detect four ArUco markers, and identified the line features distributed at the edge and the point features distributed at the center. The third part of our method performs the first stage of calibration to obtain external calibration parameters. The coplanar optimization equation was established using the corresponding relation of the 2D–3D lines, and the external parameters were estimated using the optimization algorithm. The fourth and final part of our method completed the precise optimization of the external parameters. The corresponding 2D–3D points were used to minimize the reprojection error, and further optimize the calibration results of the first stage to obtain the final external parameters.

A. CALIBRATION DEVICE DESIGN

In target-based methods, the selection of the calibration device is of substantial importance because it provides the space constraint relation required for calibration. A good calibration device design enhances the process and the results of calibration. To provide clear point and line constraints for calibration, we designed a calibration device that combined a sphere and calibration plate, as shown in Figure 3. The equipment included bright visual features and geometric features simultaneously, which was conducive to the feature extraction of images and lidar point clouds. As illustrated in the Figure 3, the device fixed a sphere at the center of the calibration plate with circular holes, and the geometric center of the calibration plate coincided with the center of the sphere. A material with high reflectivity was used on the surface of the sphere so that the lidar point cloud (projected on the sphere) had high-reflection intensity, which was conducive to the separation of the lidar point cloud distributed on the sphere. Four ArUco markers with different identities (IDs) were assigned to the four corners of the calibration plate, and the position and orientation of each mark in the camera coordinate system were calculated using OpenCV library. The design dimensions of the device are illustrated in Figure 3(a), and the processing results based on the design drawings are displayed in Figure 3(b). After the actual size measurement, the manufacturing error of the device was less than 1 mm, which meets the common criteria of the camera and lidar.
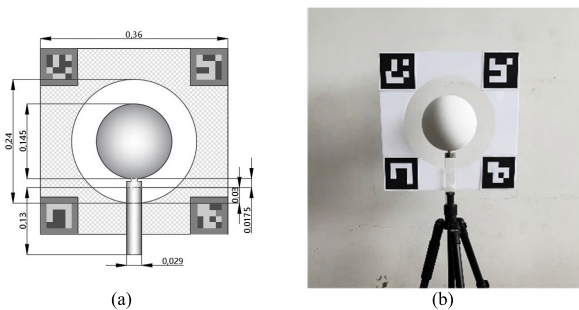

FIGURE 3. Design drawing and object of the calibration device. (a) Design drawing of the calibration device. (b) Calibration device manufactured according to design drawings.

B. IMAGE FEATURE EXTRACTION

ArUco markers are binary square markers composed of black and white blocks [21], which are often used to detect the spatial position and orientation relation between a camera and a marker. Four different ID markers were used to extract the point and line features in an image. In our study, the obtained point feature was the center of the sphere, and the line feature was located at the four edges of the calibration plate. As the camera's internal parameter matrix K and distortion parameters k_1, k_2, k_3, p_1, p_2 are known, OpenCV can be used to automatically detect the markers in the image. The four-corner pixel coordinates of each marker and its 3D position and direction in the camera coordinate system are shown in

Figure 4 (a).The pixel coordinates of the four corners of the calibration plate were extracted, and a line feature was formed between every two points. The obtained line feature was recorded as l^C, as shown in Figure 4(b). Because the spherical center coordinates coincided with the center coordinates of the calibration plate, the average position and orientation of the four markers could be calculated, and the position and orientation of the center of the calibration plate in the camera coordinate system could be obtained. The point was projected on the pixel plane, and its position was the pixel coordinate of the center of the sphere, which was recorded as p^C, as shown in Figure 4(c).
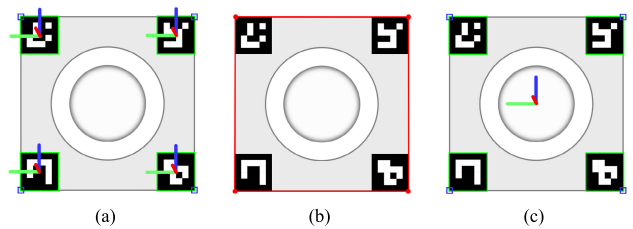
FIGURE 4. Schematic of visual feature extraction. (a) Schematic of ArUco marker detection. (b) Schematic of edge straight-line detection. (c) Schematic of spherical center-coordinate detection.

C. LIDAR POINT CLOUD FEATURE EXTRACTION

Detecting and fitting the point and line features required for calibration is the core problem of lidar point-cloud feature extraction. Therefore, a method was developed to extract automatically the point and line features of the calibration target. Before lidar point cloud feature extraction, some point cloud preprocessing was required. The spatial range of the calibration area was set according to the size of the calibration field. In this way, the point cloud on the calibration device can be adjusted to the local observation range of the lidar. Statistical filtering was applied to the point clouds within the range to filter out the outliers. The processed point cloud were mostly on the calibration device and were designated as P^{pre}.

The straight-line features required for calibration were obtained by fitting the edge point cloud onto the calibration board, and the point features were calculated by fitting the point cloud onto the sphere. Because the spatial distributions of the line and point features were different, their respective feature extraction methods were also different. The extraction of the point and line features involved independent and parallel processing. The following subsections introduce the acquisition process for the point and line features, respectively.

1) STRAIGHT-LINE FEATURE EXTRACTION

For the preprocessed point cloud P^{pre}, the plane-fitting algorithm of RANSAC [22] was used to screen the point cloud on the plane. The expected results were the plane model π of the calibration plate and the internal point cloud P^{init} on the plane. For the point cloud on the plane, the subsequent point cloud processing was facilitated by the vertical projection of

the point cloud P^{init} onto the plane π, and the subsequent recording of the projected point cloud as P^{proj}. In this task, the point cloud at the outer edge of the plane was the target to be extracted, and the α-shaped algorithm [23] extracted the contour point cloud. We set an appropriate value of $\alpha = 0.2$ as the radius and performed boundary extraction on the plane point cloud P^{proj}. The obtained edge-point cloud was designated as P^{edge}. The extraction process is illustrated in Figure 5.

The RANSAC line-fitting algorithm was used to fit the line for the obtained edge point cloud P^{edge}. Because each fitting could only obtain the equation of a straight line, the point cloud belonging to each consecutive straight line was removed, and RANSAC straight-line fitting was continued until all four spatial straight-line equations had been obtained. The line feature in the lidar coordinate system was recorded as l^L.
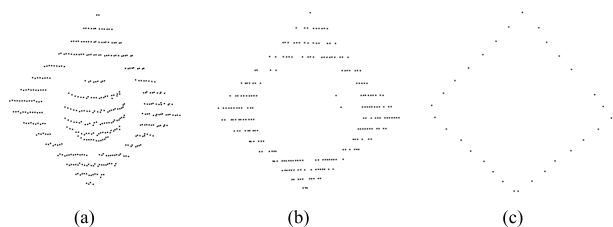

FIGURE 5. Extraction process of calibration plate-edge point cloud. (a) Preprocessed point cloud, P^{pre}. (b) Point cloud after plane projection, P^{proj}. (c) Edge-point cloud, P^{edge}.

2) POINT FEATURE EXTRACTION

Concerning the spherical point cloud extraction, we used the high-reflection intensity of the point cloud on the sphere to eliminate the aspheric point clouds in P^{pre}. We filtered the point clouds with reflection intensity less than τ, and set the value of τ to 90. By following this approach, most of the non-spherical surface point clouds were filtered, and the small number of discrete non-spherical surface point clouds were eliminated by statistical filtering. We calculated the centroid coordinates of the remaining point clouds and collected all point clouds within radius r_0 from the centroid (defined as the center), where r_0 was set between the actual radius of the sphere and the radius of the calibration plate hole. The point cloud on the surface of the sphere was designated as the final point cloud P^s. We fitted the spherical center coordinates from the point cloud P^s using a nonlinear least-squares optimization algorithm. The symbols (x_0, y_0, z_0) denote the coordinates of the center point of the sphere, and r is the radius of the sphere; the following least-squares problem was constructed according to the difference between the distance from the point to the center of the sphere and the radius of the sphere:

$$x_0, y_0, z_0, r = \underset{x_0, y_0, z_0}{argmin} \frac{1}{2} \sum_{i=1}^{N} \|r_i - r\|_2^2 \quad (1)$$

where r_i ($r_i = \sqrt{(x_i - x_0)^2 + (y_i - y_0)^2 + (z_i - z_0)^2}$) expressed the distance between the spherical center point and the

ith spatial point. Applying the derivatives of x, y, z and r with respect to (1), the Gauss–Newton algorithm was used for iterative optimization until convergence was achieved. The obtained spherical center coordinates were recorded as p^L.

D. EXTERNAL PARAMETER CALCULATION CALIBRATION OF CAMERA AND LIDAR

The lidar point cloud was relatively sparse, the point cloud near the edge of the calibration plate was noisy, and the extraction accuracy of the line features was lower than that of the point features. Therefore, to perform camera and lidar external parameter calibration from a gradual process ranging from coarse to fine, we separated our procedure into two stages: the first procedure used the edge line features of the calibration plate-edge for the initial estimation of external parameters, whereas the second procedure used the initial estimation of the external parameters as the starting point of the optimization, and further optimized the external parameters using the point features of the center of the sphere.
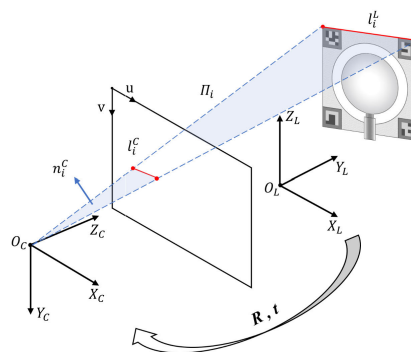

FIGURE 6. Establishment of coplanar constraints.

The corresponding 2D–3D lines were used to solve the absolute pose between the camera and lidar that constitutes a Perspective-n-Lines (PnL) problem. In the general calibration model, the constraint relations between 2–3D lines were used to establish the transformation relation between the coordinate systems. Accordingly, we established the coplanar constraint conditions for the corresponding 2D–3D lines in our study. Once these conditions were determined, as illustrated in Figure 6, the 3D line and the origin of the camera coordinate system formed a plane Π_i, with n_i^C as the normal vector of the plane. Because the 3D line l_i^L under the lidar coordinate system belongs to the plane Π_i, l_i^L is orthogonal to the normal vector n_i^C, thus forming the following constraint relationship,

$$n_i^C \cdot \left(R l_i^L + t \right) = 0 \quad (2)$$

where n_i^C is obtained by the cross-multiplication of two points on the 2D line l_i^C. With this constraint, all 2D–3D corresponding line features are introduced in (2), and the problem of solving R, t is transformed into the

following optimization problem:

$$\min_{R,t} \sum_{i=1}^{n} n_i^C \cdot \left(R l_i^L + t \right). \tag{3}$$

To solve this nonconvex optimization problem, we used the algorithm proposed in [24] in this study. When this algorithm is combined with the constraints imposed by the orthogonality of the rotation matrix, the problem is transformed into a quadratic-constrained quadratic programming problem and further relaxed into a semi-definite programming problem. By solving this problem, a unique solution for the external parameters can be obtained without a priori initial value, and the solution can be used to provide the initial external parameters of the cameras and lidars.
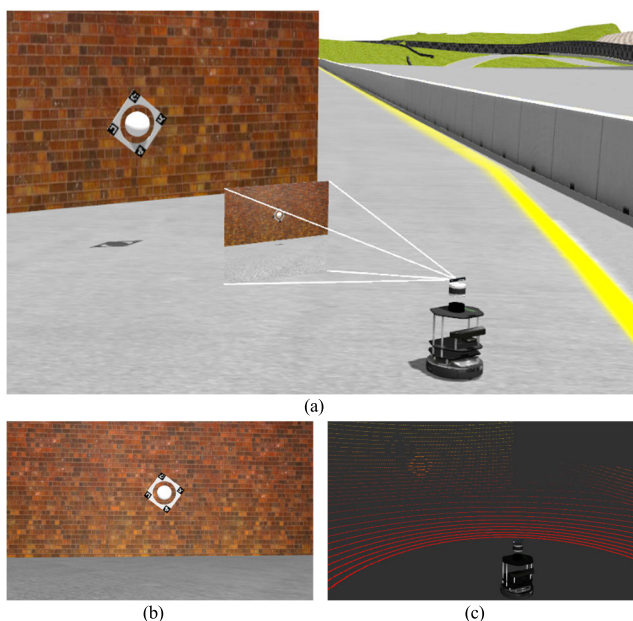
FIGURE 7. Simulation experiment platform and scene settings. (a) Calibration scene generated in Gazebo. (b) Images captured by the camera. (c) Point clouds collected by the lidar.

To obtain the external parameters with higher accuracy, it is necessary to continue optimizing the initial external parameters. The correspondence of the 2D–3D points was used here to minimize the reprojection error and construct the following nonlinear least-squares problem,

$$\xi = \arg\min_{\xi} \frac{1}{2} \sum_{i=1}^{n} \left\| p_i^C - K \exp\left(\xi^\wedge\right) p_i^L \right\|_2^2 \tag{4}$$

where ξ is a member of an $se(3)$ Lie algebra, expressed in the form of a six-dimensional vector representing the rotation and translation. The operator $exp(\cdot)$ expresses the process of mapping an $se(3)$ Lie algebra to an $SE(3)$ Lie group based on an exponential transformation, representing a transformation from a vector to a matrix. K is the internal parameter of the camera. The nonlinear optimization problem is solved with the initial external parameters by calculating the Jacobian matrix of (4) and using the Levenberg–Marquardt algorithm.

IV. EXPERIMENTS AND RESULTS

The true values of the external parameters associated with the real camera and lidar cannot be determined easily; this is usually not conducive to the evaluation of the accuracy of the external parameters. However, in virtual simulation technology, external parameters may be selected arbitrarily; therefore, the use of a simulation may test the performance of the calibration in many aspects. Accordingly, we assessed the methods employed in this study in a virtual simulation environment as well as an actual environment. The simulation experimental design is illustrated in Figure 7. In Figure 7(a), we illustrate the calibration scene created in the Gazebo simulation software. The spatial relationship between the camera and the lidar sensor can be set as $(-90, 0, -90, -0.046, 0.066, 0)$, where the Euler angle is in degrees and the translation is in meters. The resolution of the camera was 640×480 pixels. The camera was set as a pinhole model, and its internal parameters have been estimated by Zhang's calibration method [25]. The lidar simulated the VLP-32C sensor, which has 32 channels and a 360° horizontal field-of-view.

In the actual experiment, all the sensors were integrated into an unmanned vehicle. Figure 8 shows the experimental platform and scene design of the actual experiment. The Velodyne VLP-32C lidar responsible for scanning the point cloud was installed on the top of the unmanned vehicle, as shown in Figure 8 (b), and the lidar specifications were shown in Table 1. The Realsense D435 camera was fixed under the lidar, as shown in Figure 8 (c), and the camera specifications were shown in Table 2.

TABLE 1. Specifications of the VLP-32C lidar.

Parameter	Value
Channel	32
Measurement Range	200m
Range Accuracy	±3cm
Field of View (Vertical)	-25° to +15°(40°)
Horizontal Angle Resolution	0.1° - 0.4°
Rotation Frequency	5 Hz - 20 Hz

TABLE 2. Specifications of the Realsense D435 camera.

Parameter	Value
Resolution	640×480
Pixel Size	3μm×3μm
Frame Rate	30FPS
Field of View	69°×42°(±1°)

A. SIMULATION EXPERIMENTS

In the design of the calibration experiment simulation, the camera and lidar sensor were simulated in accordance with the actual sensor parameters, and the simulated camera and lidar sensor were jointly associated with the turnelbot2 [26] mobile robot. After the calibration device was fixed, the robot position was moved slowly and evenly to procure the data.
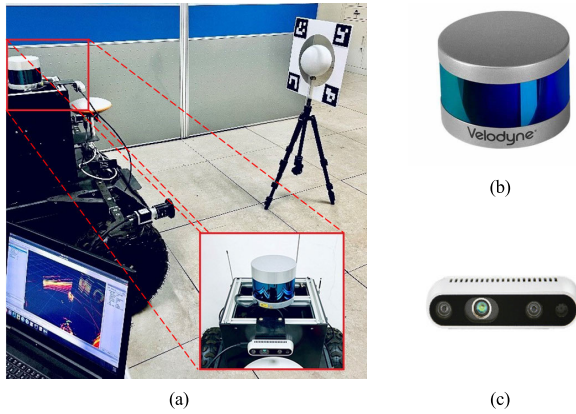
FIGURE 8. Real experiment settings. (a) Camera and lidar system in the experiment. (b) VLP-32C lidar. (c) Realsense D435 camera.
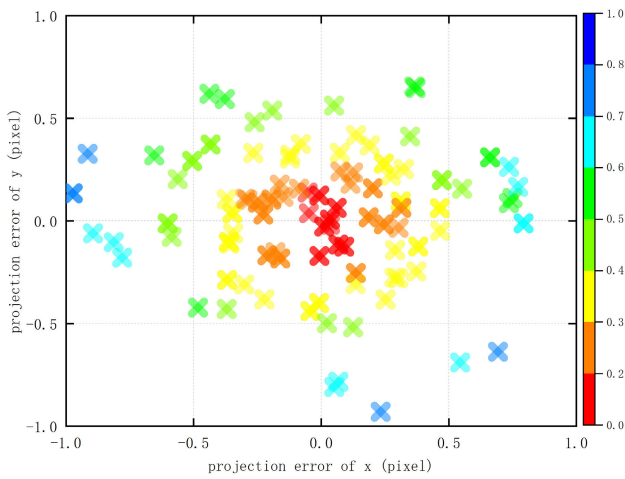

FIGURE 9. Distribution of reprojection error.

In this experiment, we assembled 80 frames of experimental data from multiple angles for calibration and compared the external parameter results with the reference (true) values. The results are listed in Tables 3 and 4, where the rotation term is expressed in the form of Euler angles, and Ground Truth is the reference (true) values.

TABLE 3. Calibration results of rotation term in simulation experiment.

	Rotation part (°)			Average error (°)
	roll	pitch	yaw	
Ground truth	-90	0	-90	-
Initial value	-89.268	0.161	-91.693	0.862
Optimization value	-90.117	-0.024	-90.069	0.07

As shown in Tables 3 and 4, the average errors of rotation and translation of the initial external parameters were 0.862° and 0.079 m, respectively, whereas those of the optimized external parameters were 0.07° and 0.011 m, respectively. For both the translation and rotation parts, the error of the optimized value was less than that of the initial value, and the

TABLE 4. Calibration results of translation term in simulation experiment.

	Translation part (m)			Average error (m)
	x	y	z	
Ground truth	-0.046	0.066	0	-
Initial value	0.083	0.017	-0.06	0.079
Optimization value	-0.028	0.063	-0.012	0.011

optimized value was very close to the reference (true) value, thus demonstrating that the external parameters obtained by the method adopted in this study achieved a high degree of accuracy. In the first stage of calibration, the accuracy of the external parameters obtained was limited but sufficiently high to guide the subsequent optimization process successfully.

The average reprojection error is an important criterion for evaluating the calibration results. Each 3D spherical center point was inversely calculated based on the external parameters to obtain 2D projection points, and the average Euclidean distance between each 2D projection point and the known 2D spherical center point was calculated as follows,

$$\bar{e} = \frac{1}{n} \sum_{i=1}^{n} \sqrt{(u_i - u_i')^2 + (v_i - v_i')^2} \tag{5}$$

where (u_i, v_i) are 2D projection points, and (u_i', v_i') are known 2D point coordinates. According to (5), the average reprojection error of this experiment was 0.45 pixels; this corresponds to a satisfactory calibration quality. The error distribution is shown in Figure 9.

To assess the accuracy of the calibration results intuitively, all lidar point clouds were projected onto the image using the final external parameters and the internal camera parameters. The results of the reprojection are illustrated in Figure 10. We assigned different colors according to the depth distance of the point cloud, which is more conducive to observing the alignment between the point cloud and the image. From the projection renderings of the two scenes, it is clear that the projection effect of the point cloud was highly accurate, thus proving that the external parameters calculated by the method adopted in this study were reliable.
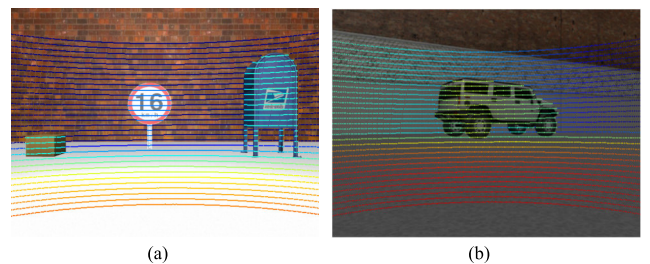

FIGURE 10. Rendering of simulation experiment reprojection.

To verify the accuracy of the method in this study, we compared the Autoware [27] and Park et al. [17], Dhall et al. [5], and Zhou's methods [28]. The results are listed in Table 5.

TABLE 5. External parameter residual and reprojection error compared to other calibration methods.

| Calibration Method	Δroll (°)	Δpitch (°)	Δyaw (°)	Δx (m)	Δy (m)	Δz (m)	ΔR(°)	Δt (m)	MRE (pixel)
Ours	-0.117	-0.024	-0.069	0.017	-0.003	-0.012	0.070	0.011	0.45
Autoware	1.606	0.135	1.131	0.091	0.033	-0.038	0.957	0.054	3.25
Park	0.257	0.120	0.817	0.066	-0.101	-0.072	0.398	0.080	3.02
Dhall	-0.217	0.333	-0.180	0.017	-0.035	0.058	0.243	0.037	1.70
Zhou	0.013	-0.037	-0.471	0.051	0.002	-0.014	0.174	0.022	0.78

We used Euler angles to express the external parameters, and calculated the error between each external parameter and the true value. ΔR is the average error of the rotation part, Δt is the average error of the translation part, and MRE is the average reprojection error. As shown in Table 5, the precision of external parameters obtained by the method proposed in this study is higher than that of other methods; this finding justifies the high-precision features of this method.

B. INFLUENTIAL FACTORS IN SIMULATION EXPERIMENTS

In this subsection, we describe how we tested the calibration performance subject to the influence of different factors by simulating a set of variable factors, such as lidar noise, lidar model, and observation distance, in the simulation environment. We evaluated the differences between the true values of the external parameters obtained by varying the values of the different factors. To test the influence of each factor on the calibration efficiency, the experiment was set up as follows: the standard deviation of the laser noise, σ, was set to 0.03 m, the number of laser radar harnesses was set to 32, and the observation distance was set to 2–4 m. The effects of these factors were assessed one at a time, while the other two factors remained unchanged.

First, we assessed the influence of laser noise on the calibration results by applying Gaussian noise to the lidar sensor with a mean value of zero and standard deviations equal to 0.02 m, 0.04 m, and 0.06 m, respectively. We designed three corresponding groups. Each group performed 10 independent calibrations and randomly acquired 18 frames of synchronous data for each calibration. The error distribution of the test results is shown in Figure 11, where the yellow dot represents the average value, and the red line represents the median. An increase in the laser noise caused a slight increase in the error of the external parameters. However, the average errors of the rotation term and the shift term remained within $0 – 0.2°$ and $0.02 – 0.04$ m, respectively, which reflects a good calibration result, indicating that the method adopted in this study was stable against changes in the noise resistance.

Second, we assessed the effect of changing the number of laser radar harnesses on the calibration results. We simulated laser radars with 16, 32, and 64 harnesses. We designed three corresponding groups of experiments. Each group of experiments contained 10 independent calibrations, and 18 frames of synchronous data were randomly collected for each calibration. The error distribution of the test results is shown
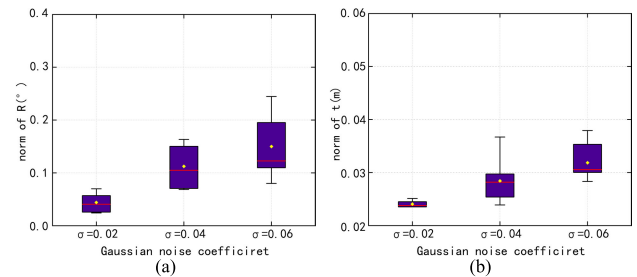
FIGURE 11. Influence of laser noise on external parameter accuracy. (a) Error distribution diagram of rotation term. (b) Error distribution diagram of translation term.

in Figure 12, where the yellow dot represents the average value, and the red line represents the median. It is clear from the error distribution diagram that the calibration errors obtained for the three groups of experiments were stable against changes in the number of harnesses and that a high level of accuracy was maintained; these findings demonstrate that the adopted method is compatible with a variety of mainstream laser radars and cameras for calibration.
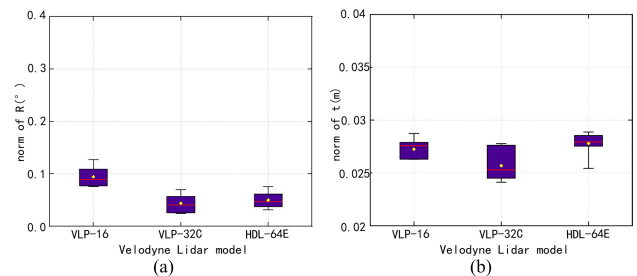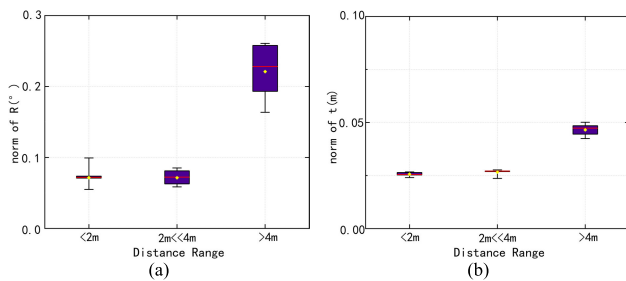

FIGURE 12. Influence of the number of laser radar harnesses on the accuracy of external parameter calibration. (a) Error distribution diagram of rotation term. (b) Error distribution diagram of translation term.

Finally, we assessed the effect of changing the observation distance on the calibration results. Three groups of experiments were designed according to the distance between the calibration device and the sensor platform. The observation distance from the sensor platform to the calibration device was set to <2 m, 2 – 4 m, and >4 m, respectively. Each group performed 10 independent calibrations and randomly collected 18 frames of synchronous data for each calibration. The error distribution of the test results is shown in Figure 13, where the yellow dot represents the average value, and the red line represents the median. It is clear that our method has very

small rotation and translation errors when the observation distance is less than 4m. The rotation and translation average errors were around 0.1° and 0.03m. whereas the average error increased when the distance exceeded 4 m. However, the rotation and translation average errors increased to about 0.2° and 0.05m when the distance exceeded 4 m. Actually, the degradation of calibration accuracy was unavoidable because of the limited size of the calibration device. On the one hand, the farther the observation distance, the thinner point cloud on the calibration device, thus affecting the fitting accuracy of point cloud. On the other hand, the camera's observation of the calibration device is not sufficiently fine to accommodate an increase in the observation distance, leading to a visual extraction error. Therefore, to ensure the accuracy of the calibration results, the observation distance should be maintained within 4 m.

FIGURE 13. Effect of observation distance on external parameter accuracy. (a) Error distribution diagram of rotation term. (b) Error distribution diagram of translation term.

C. REALISTIC EXPERIMENTS

The preceding two subsections included an account of our assessment of the stability and accuracy of the adopted method in simulation experiments. In this subsection, we discuss the calibration and testing of the method on a real experimental platform. However, the true values of the external parameters between the camera and lidar are not measurable in actual experiments; therefore, it is difficult to analyze the errors in the external parameters. We determined the accuracy of the external parameters of the real experiment using plane projection rendering of the point cloud. Because the observation distance should not be too large, this experiment was calibrated in flat space, and 18, 36, and 54 groups of synchronous frame data, respectively, were collected for the calibration experiment. Three sets of experimental data were calibrated. The results obtained for the external parameters and the mean reprojection error (MRE) are listed in Table 6. The differences in the values of the external parameters estimated by the three groups of experiments are very small, and the average reprojection error was approximately 1 pixel, thus indicating that accurate external parameters can be calculated using only 18 groups of synchronized frame data. Using the average external parameters of the three groups of experiments as the final calibration results, the point clouds of the three groups of different scenes were projected onto
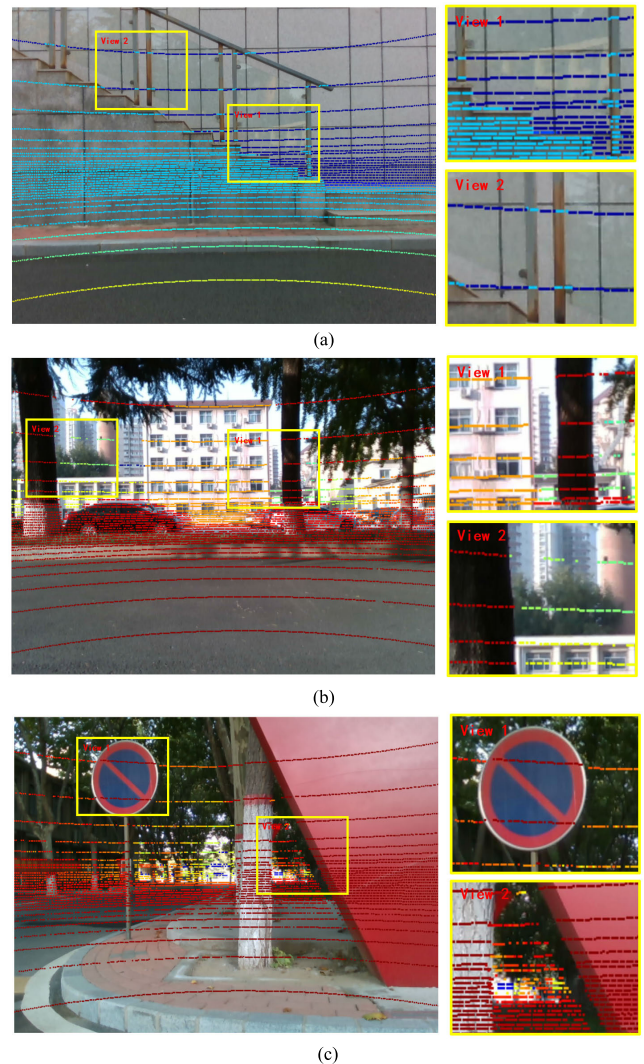
FIGURE 14. Effect picture of point-cloud reprojection on the image. (a), (b), and (c) are three actual outdoor scenes.

the corresponding images. The projection effects are shown in Figure 14(a), 14(b), and 14(c). The color of the point cloud varies according to its depth. The accuracy of the projection is assessed based on the color difference of the point clouds of nearby and distant objects. As illustrated in the figure, the actual depth of the point cloud is consistent with the distant and nearby distribution of objects in the image, thus yielding a satisfactory projection effect in the enlarged view. These results confirm that the values of the external parameters calculated by our method are highly accurate.

V. DISCUSSION

Overall, we proposed a two-stage calibration method based on a calibration device that aimed to obtain high-precision external parameters of a camera and lidar. In the simulation environment, we compared this method with other target-based methods based on 80 observations. The results in Table 3 showed that our method has obvious advantages

TABLE 6. Realistic experimental calibration results of three groups of synchronous frame data.

Frame(s)	N=18	N=36	N=54
roll (°)	-89.556	-89.563	-89.566
pitch (°)	1.002	0.989	0.991
yaw (°)	139.171	139.171	139.173
x (m)	0.022	0.021	0.021
y (m)	-0.046	-0.050	-0.051
z (m)	-0.146	-0.155	-0.156
MRE (pixel)	1.05	1.01	1.01

in calibration accuracy. Using the Autoware method [27] required manual extraction of the normal vector of a chessboard. However, manual operation had certain instability, which leads to poor results. Dhall's and Park's method [5], [17] realized the automatic extraction of the edge features from a chessboard, but these features were vulnerable to the interference of laser noise, which affected the calibration result. Considering the limitations of the aforementioned methods, we adopted two different features for calibration. The sphere had proved to be a robust calibration target [20]. Therefore, the accuracy and stability of calibration can be effectively improved by combining both planar and spherical features. This view was verified in Section IV-B.

However, the methods proposed in this study also have some limitations:

1) Due to the limited size of the calibration device, too far observation distance will lead to deviation in feature extraction, which will lead to inaccurate calibration. Therefore, the use of this method is usually limited to a specific calibration space, and this mode is more applicable to factory calibration of multi-sensor equipment.

2) The method in this study is an offline calibration method. Given that the fusion technology of camera and lidar is widely used in the autopilot field, we will try to achieve online calibration in the future [29], [30], [31].

3) The calibration parameters will be invalid if they are acted by external forces during the operation of the multi-sensor platform. In the future, the identification of ways to monitor the external parameter changes and execution of online tuning will be considered extensively.

VI. CONCLUSION

In this study, we proposed a high-precision external parameter calibration method for a camera and lidar based on a common calibration device. The corresponding point and line features were automatically extracted from the image and the laser point cloud, respectively. The initial values of the external parameters were determined using the edge-line feature, and the initial external parameters were optimized using the center point of the sphere. Based on two-stage calibration (ranging from coarse to fine), the external parameters were accurately calculated without prior initial values; this enhanced the robustness of the calibration system.

The method was tested in simulation and real environments, respectively, and accurate external parameters

between the camera and lidar were obtained. In addition, compared with the state-of-the-art, our method has advantages in terms of accuracy. The effects of several factors on the calibration results were tested in a simulated environment. The experimental results showed that the method can be applicable to multiple lidar sensors with different harness channels, and is robust to laser noise, which reflects the stability of the calibration system.

REFERENCES

[1] G. Pandey, J. McBride, S. Savarese, and R. Eustice, "Extrinsic calibration of a 3D laser scanner and an omnidirectional camera," *IFAC Proc. Volumes*, vol. 43, no. 16, pp. 336–341, 2010.

[2] P. An, T. Ma, K. Yu, B. Fang, J. Zhang, W. Fu, and J. Ma, "Geometric calibration for LiDAR-camera system fusing 3D–2D and 3D–3D point correspondences," *Opt. Exp.*, vol. 28, no. 2, pp. 2122–2141, 2020.

[3] L. Yin, B. Luo, W. Wang, H. Yu, C. Wang, and C. Li, "CoMask: Corresponding mask-based end-to-end extrinsic calibration of the camera and LiDAR," *Remote Sens.*, vol. 12, no. 12, p. 1925, Jun. 2020.

[4] X. Gong, Y. Lin, and J. Liu, "3D LIDAR-camera extrinsic calibration using an arbitrary trihedron," *Sensors*, vol. 13, no. 2, pp. 1902–1918, 2013.

[5] A. Dhall, K. Chelani, V. Radhakrishnan, and K. M. Krishna, "LiDAR-camera calibration using 3D–3D point correspondences," 2017, *arXiv:1705.09785*.

[6] M. Pereira, D. Silva, V. Santos, and P. Dias, "Self calibration of multiple LIDARs and cameras on autonomous vehicles," *Robot. Auton. Syst.*, vol. 83, pp. 326–337, Sep. 2016.

[7] Z. Taylor and J. Nieto, "Motion-based calibration of multimodal sensor arrays," in *Proc. IEEE Int. Conf. Robot. Autom. (ICRA)*, May 2015, pp. 4843–4850.

[8] A. Mastin, J. Kepner, and J. Fisher, "Automatic registration of LiDAR and optical images of urban scenes," in *Proc. IEEE Conf. Comput. Vis. Pattern Recognit.*, Jun. 2009, pp. 2639–2646.

[9] J. Castorena, U. S. Kamilov, and P. T. Boufounos, "Autocalibration of LiDAR and optical cameras via edge alignment," in *Proc. IEEE Int. Conf. Acoust., Speech Signal Process. (ICASSP)*, Mar. 2016, pp. 2862–2866.

[10] G. Iyer, R. K. Ram, J. K. Murthy, and K. M. Krishna, "CalibNet: Geometrically supervised extrinsic calibration using 3D spatial transformer networks," in *Proc. IEEE/RSJ Int. Conf. Intell. Robots Syst. (IROS)*, Oct. 2018, pp. 1110–1117.

[11] R. Ishikawa, T. Oishi, and K. Ikeuchi, "LiDAR and camera calibration using motions estimated by sensor fusion odometry," in *Proc. IEEE/RSJ Int. Conf. Intell. Robots Syst. (IROS)*, Oct. 2018, pp. 7342–7349.

[12] J. Kang and N. L. Doh, "Automatic targetless camera–LiDAR calibration by aligning edge with Gaussian mixture model," *J. Field Robot.*, vol. 37, no. 1, pp. 158–179, Jan. 2020.

[13] G, Pandey, J. R. McBride, S. Savarese, and R. M. Eustice, "Automatic targetless extrinsic calibration of a 3D LiDAR and camera by maximizing mutual information," in *Proc. 26th AAAI Conf. Artif. Intell.*, 2012, pp. 1–7.

[14] X. Lv, B. Wang, Z. Dou, D. Ye, and S. Wang, "LCCNet: LiDAR and camera self-calibration using cost volume network," in *Proc. IEEE/CVF Conf. Comput. Vis. Pattern Recognit. Workshops (CVPRW)*, Jun. 2021, pp. 2894–2901.

[15] W. Wang, K. Sakurada, and N. Kawaguchi, "Reflectance intensity assisted automatic and accurate extrinsic calibration of 3D LiDAR and panoramic camera using a printed chessboard," *Remote Sens.*, vol. 9, no. 8, p. 851, Aug. 2017.

[16] D. Tsai, S. Worrall, M. Shan, A. Lohr, and E. Nebot, "Optimising the selection of samples for robust lidar camera calibration," in *Proc. IEEE Int. Intell. Transp. Syst. Conf. (ITSC)*, Sep. 2021, pp. 2631–2638.

[17] Y. Park, S. Yun, C. S. Won, K. Cho, K. Um, and S. Sim, "Calibration between color camera and 3D LIDAR instruments with a polygonal planar board," *Sensors*, vol. 14, no. 3, pp. 5333–5353, 2014.

[18] Z. Pusztai and L. Hajder, "Accurate calibration of LiDAR-camera systems using ordinary boxes," in *Proc. IEEE Int. Conf. Comput. Vis. Workshops (ICCVW)*, Oct. 2017, pp. 394–402.

[19] J. Beltran, C. Guindel, A. de la Escalera, and F. García, "Automatic extrinsic calibration method for LiDAR and camera sensor setups," *IEEE Trans. Intell. Transp. Syst.*, vol. 23, no. 10, pp. 17677–17689, Oct. 2022.

[20] T. Toth, Z. Pusztai, and L. Hajder, "Automatic LiDAR-camera calibration of extrinsic parameters using a spherical target," in *Proc. IEEE Int. Conf. Robot. Autom. (ICRA)*, May 2020, pp. 8580–8586.

[21] S. Garrido-Jurado, R. Muñoz-Salinas, F. J. Madrid-Cuevas, and M. J. Marín-Jiménez, "Automatic generation and detection of highly reliable fiducial markers under occlusion," *Pattern Recognit.*, vol. 47, pp. 2280–2292, Jun. 2014.

[22] B. Oehler, J. Stueckler, J. Welle, D. Schulz, and S. Behnke, "Efficient multi-resolution plane segmentation of 3D point clouds," in *Proc. Int. Conf. Intell. Robot. Appl.*, 2011, pp. 145–156.

[23] H. Edelsbrunner and E. P. Mücke, "Three-dimensional alpha shapes," *ACM Trans. Graph.*, vol. 13, no. 1, pp. 43–72, 1994.

[24] S. Agostinho, J. Gomes, and A. Del Bue, "CvxPnPL: A unified convex solution to the absolute pose estimation problem from point and line correspondences," *J. Math. Imag. Vis.*, 2022, doi: 10.1007/s10851-022-01133-8.

[25] Z. Zhang, "A flexible new technique for camera calibration," *IEEE Trans. Pattern Anal. Mach. Intell.*, vol. 22, no. 11, pp. 1330–1334, 2000.

[26] H. I. M. A. Omara and K. S. M. Sahari, "Indoor mapping using Kinect and ROS," in *Proc. Int. Symp. Agents, Multi-Agent Syst. Robot. (ISAMSR)*, Aug. 2015, pp. 110–116.

[27] S. Kato, S. Tokunaga, Y. Maruyama, S. Maeda, M. Hirabayashi, Y. Kitsukawa, A. Monrroy, T. Ando, Y. Fujii, and T. Azumi, "Autoware on board: Enabling autonomous vehicles with embedded systems," in *Proc. ACM/IEEE 9th Int. Conf. Cyber-Phys. Syst. (ICCPS)*, Apr. 2018, pp. 287–296.

[28] L. Zhou, Z. Li, and M. Kaess, "Automatic extrinsic calibration of a camera and a 3D LiDAR using line and plane correspondences," in *Proc. IEEE/RSJ Int. Conf. Intell. Robots Syst. (IROS)*, Oct. 2018, pp. 5562–5569.

[29] S. Wang, X. Zhang, G. Zhang, Y. Xiong, G. Tian, S. Guo, J. Li, P. Lu, J. Wei, and L. Tian, "Temporal and spatial online integrated calibration for camera and LiDAR," in *Proc. IEEE 25th Int. Conf. Intell. Transp. Syst. (ITSC)*, Oct. 2022, pp. 3016–3022.

[30] W. Wang, S. Nobuhara, R. Nakamura, and K. Sakurada, "SOIC: Semantic online initialization and calibration for LiDAR and camera," 2020, *arXiv:2003.04260*.

[31] H. Xu, G. Lan, S. Wu, and Q. Hao, "Online intelligent calibration of cameras and LiDARs for autonomous driving systems," in *Proc. IEEE Intell. Transp. Syst. Conf. (ITSC)*, Oct. 2019, pp. 3913–3920.

YING YU received the Ph.D. degree in photogrammetry and remote sensing from PLA Information Engineering University, Zhengzhou, China, in 2014. He is currently a Master's Supervisor with PLA Information Engineering University. He has long been engaged in teaching and scientific research in remote sensing image interpretation and intelligent processing. His research interests include remote sensing, image intelligent processing, and robotics.

MAOLIN XU received the M.S. degree from Liaoning Technical University, Fuxin, China, in 2004. He is currently a Master's Supervisor with PLA Information Engineering University. He is also a Professor with the University of Science and Technology Liaoning. His research interests include indoor positioning and digital 3D modeling.

SONG FAN received the B.S. degree in surveying and mapping engineering from the University of Science and Technology Liaoning, Anshan, China, in 2020, where he is currently pursuing the M.S. degree. His research interests include robotic localization and sensor fusion.

LONGHAI ZHAO received the B.S. degree in geodetic surveying from PLA Information Engineering University, Zhengzhou, China, in 2007. His research interests include autonomous spatial data acquisition and photogrammetry.

• • •